Towards vibrational spectroscopy on surface-attached colloids performed with a quartz crystal microbalance

CrossMark

Diethelm Johannsmann *

Institute of Physical Chemistry, Clausthal University of Technology, Germany

ABSTRACT

Colloidal spheres attached to a quartz crystal microbalance (QCM) produce the so-called "coupled resonances". They are resonators of their own, characterized by a particle resonance frequency, a resonance bandwidth, and a modal mass. When the frequency of the main resonator comes close to the frequency of the coupled resonance, the bandwidth goes through a maximum. A coupled resonance can be viewed as an absorption line in acoustic shear-wave spectroscopy. The known concepts from spectroscopy apply. This includes the mode assignment problem, selection rules, and the oscillator strength. In this work, the mode assignment problem was addressed with Finite Element calculations. These reveal that a rigid sphere in contact with a QCM displays *two* modes of vibration, termed "slipping" and "rocking". In the slipping mode, the sphere rotates about its center; it exerts a tangential force onto the resonator surface at the point of contact. In the rocking mode, the sphere rotates about the point of contact; it exerts a torque onto the substrate. In liquids, both axes of rotation are slightly displaced from their ideal positions. Characteristic for spectroscopy, the two modes do not couple to the mechanical excitation equally well. The degree of coupling is quantified by an oscillator strength. Because the rocking mode mostly exerts a torque (rather than a tangential force), its coupling to the resonator's tangential motion is weak; the oscillator strength consequently is small. Recent experiments on surface-adsorbed colloidal spheres can be explained by the mode of vibration being of the rocking type.

1. Introduction

The quartz crystal microbalance is well known to the scientific community as a film thickness monitor [1] and, further, as a tool to study of soft layers beyond gravimetry [2,3]. Central to the advanced QCM is the ability to determine the resonance bandwidth in addition to resonance frequency and to compare shifts of frequency and bandwidth between overtones [4]. The models of stratified viscoelastic layer systems on a QCM surface are well-established [5,6].

Many samples of practical interest are not stratified layers. This includes particles [7–9], cell layers [10], vesicles [11], viruses [12,13], and bacteria [14–16]. Generally speaking, the prediction of the shifts in frequency and bandwidth (Δf and $\Delta \Gamma$) induced by structured samples is challenging. Numerical methods are required [17]. There is one group of heterogeneous samples, though, which *is* amenable to analytical description. If the particle of interest contacts the resonator surface across a sufficiently narrow contact (a "point contact"), and if, further, neighboring contacts are elastically independent from each other, the only parameters of relevance are the tangential force and the torque. Since the zone of deformation is small, one can define a tangential displacement and an angle of rotation, to be evaluated far away from the

deformed zone (Fig. 1A). The deformed region in the following is called "the contact". The fact that the contact is localized is critical to the analysis.

In the past, the complications arising from the motion of the external object being a superposition of translation and rotation have often been avoided by choosing the external objects so heavy that they were clamped in space by inertia [18,19]. Large spheres do not follow the MHz oscillation of the resonator, they undergo neither rotation nor translation. The angle of rotation then is zero; the displacement between the two sides of the contact is equal to the displacement of the resonator surface, given as $u_0\cos(\omega t)$ with u_0 the amplitude of oscillation. Dividing force by displacement, one obtains the contact's tangential stiffness.

The arguments below are concerned with situations, where the external object is too small to be clamped in space. Most bio-colloids fall into that class. The prospect of being able to measure the stiffness of a link between a bio-colloid and a solid substrate has attracted much interest. The situation evidently becomes more complicated than for large immobile spheres, but as long as the object is stiff, translation and rotation can be accounted for with suitably modified equations.

Particles in the micron-size range give rise to a phenomenon known since 1985, which is the "coupled resonance" [20]. (Coupled resonances were known before, but they were put into the context of QCM-based sensing by Dybwad at that time.) An introduction to coupled resonances

* Corresponding author.
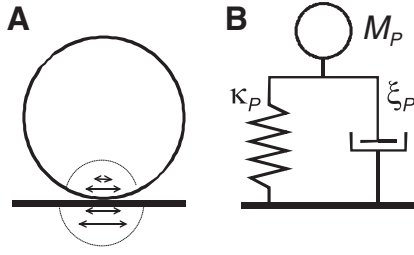 E-mail address: johannsmann@pc.tu-clausthal.de.

Fig. 1. A: Sketch of a contact between a sphere and the resonator surface. It is essential that the contact is smaller than the sphere and, also, is smaller than the wavelength of sound. Only the region close to the contact (dashed circle) is deformed. Together with the deformed region of the substrate, it forms a Hookean spring. B: Mechanical equivalent circuit. Viscous dissipation is accounted for by a dashpot.

is given in Section 2. It turns out that a coupled resonance amounts to an absorption line in shear-wave spectroscopy. A particle linked to the surface has its own frequency of vibration. With a QCM, one can do vibrational spectroscopy on surface-attached colloids. The conceptual analogies between coupled resonances and shear-wave spectroscopy are far-reaching. Keywords are mode-assignment, modal mass, modal stiffness, homogeneous linewidth, heterogeneous linewidth, degeneracy, selection rules, and oscillator strength. These terms can all be applied to shear-wave spectroscopy. The oscillator strength, in particular, is non-trivial. The oscillator strength is needed to explain experimental results.

A complication not appreciated by Dybwad was the fact that there are (at least) two dynamic variables, which are the position of the particle along the direction of surface displacement and the angle of rotation into the same direction. The conjugate variables are a tangential force and a torque. Because there are two dynamic variables, there are two coupled resonances. Dybwad's model misses this aspect. He depicts the geometry as one-dimensional. The way he draws his central diagram alludes to rotation, but he does not elaborate. The following discussion closes this gap.

2. Coupled resonances

Central to the prediction of the frequency shift is the small-load approximation, which states that the complex frequency shift ($\Delta\tilde{f} = \Delta f + i\Delta\Gamma$, with Γ the half-bandwidth at half-height) is proportional to the load impedance, Z_L. The load impedance is the area-averaged ratio of stress and velocity at the resonator surface. We have:

$$\frac{\Delta\tilde{f}}{f_F} = \frac{\Delta f + i\Delta\Gamma}{f_F} \approx \frac{i}{\pi Z_q}\left\langle\frac{\tilde{\sigma}_0}{\tilde{v}_0}\right\rangle_{area} = \frac{i}{\pi Z_q}\tilde{Z}_L \tag{1}$$

A tilde denotes a complex variable and an index 0 denotes a complex amplitude of a time-harmonic variable. Γ (the half-bandwidth) is related to the widely used "dissipation factor" [21], D, by the relation $D = 2\Gamma/f$. f_F is the fundamental frequency, $Z_q = 8.8 \cdot 10^6$ kg m^{-2} s^{-1} is the acoustic wave impedance of AT-cut quartz. σ is the tangential stress, v is the tangential velocity, and $Z_L \leq \tilde{\sigma}_0/\tilde{v}_0 >$ is the load impedance (the ratio of stress and velocity). Angle brackets denote an area average.

For discrete contacts, the load impedance can be expressed as N_P/A $\tilde{F}_0/\tilde{v}_0 = N_P/A\, Z_{mech}$ with N_P the number of particles and A the active area, $\tilde{F}_0$ the amplitude of the periodic force exerted at the contact, and Z_{mech} the mechanical impedance of the sphere in contact with the surface (the force-to-velocity ratio, see below). In the following discussion, we exploit the electromechanical analogy. The sphere-plate assembly can be modeled by a mechanical equivalent circuit as depicted in Fig. 1B. The force exerted by an arrangement of dashpots, springs, and point-masses follows from the mechanical impedances of the individual elements and certain rules of how to add impedances together. These

rules are the analogs of the Kirchhoff rules in electrical engineering. There is a complication with regard to the mechanical Kirchhoff rules: In mechanical circuits, impedances are additive if the elements are placed in parallel, while inverse impedances are additive if the elements are placed in series. In this regard, the rules differ from electricity, where impedances are additive for elements arranged in series. The mechanical impedances entering the problem are $i\omega M_P$, (originating from a rigid point-mass M_P), $\kappa_P/(i\omega)$ with κ_P the spring constant of a Hookean spring, and ξ_P, where ξ_P is the drag coefficient of a dashpot. κ_P, ξ_P, and M_P will have to be interpreted as a modal stiffness, a modal damping, and a modal mass later on. The meaning of these parameters depends on the mode of vibration. At this point, we assume κ_P, ξ_P, and M_P to be the same for all spheres, that is, we ignore heterogeneity. Also, κ_P and ξ_P might depend on frequency, but we treat them as constant for simplicity. κ_P is also called "contact stiffness" in the following. Note that this definition pertains to an individual contact (as opposed to the stiffness of an interface between rough surfaces).

Representing a particle in contact with the resonator surface by an equivalent circuit as in Fig. 1B, one finds the load impedance as

$$\tilde{Z}_L = \frac{N_P}{A}\left(\left(\frac{\kappa_P}{i\omega} + \xi_P\right)^{-1} + (i\omega M_P)^{-1}\right)^{-1} = \frac{N_P}{A}\left(\left(\frac{\tilde{\kappa}_P}{i\omega}\right)^{-1} + (i\omega M_P)^{-1}\right)^{-1}$$
$$= \frac{N_P}{A}\,\frac{i\omega M_P\tilde{\kappa}_P}{\tilde{\kappa}_P - \omega^2 M_P} \tag{2}$$

In step 2, the spring constant and the drag coefficient were subsumed under a single complex spring constant, $\tilde{\kappa}_P$, given as $\tilde{\kappa}_P = \kappa_P + i\omega\xi_P$. Inserting Eq. (2) into Eq. (1), one finds

$$\frac{\Delta\tilde{f}}{f_F} = \frac{N_P}{A}\frac{-\omega M_P}{\pi Z_q}\frac{\tilde{\kappa}_P}{\tilde{\kappa}_P - \omega^2 M_P} = \frac{N_P}{A}\frac{-\omega M_P}{\pi Z_q}\frac{\kappa_P + i\omega\xi_P}{\kappa_P + i\omega\xi_P - \omega^2 M_P} \tag{3}$$

Eq. (3) can be simplified by introducing the "particle resonance frequency", $\tilde{\omega}_P$, as

$$\tilde{\omega}_P^2 = 4\pi^2\tilde{f}_P^2 = \frac{\tilde{\kappa}_P}{M_P} = \frac{\kappa_P}{M_P} + \frac{i\omega\xi_P}{M_P} = \omega_P^2 + i\omega\gamma_P \tag{4}$$

In the last step, the damping factor was introduced, which is defined as $\gamma_P = \xi_P/M_P$. γ_P has dimensions of frequency. If the damping of the coupled resonance is small (only then), $\gamma_P/(2\pi)$ is equal to the bandwidth of the coupled resonance (see Fig. 2). One can then write $\tilde{\omega}_P \approx \omega_P + i\gamma_P/2$ close to the resonance. To see that, write

$$\tilde{\omega}_P = \omega_P\sqrt{1 + \frac{i\omega\gamma_P}{\omega_P^2}} \approx \omega_P\left(1 + \frac{i\omega\gamma_P}{2\omega_P^2}\right) \approx \omega_P + \frac{i\gamma_P}{2} \tag{5}$$

Taylor-expansion of the square root was used in step 2; $\omega \approx \omega_P$ was used in step 3. For narrow resonances, the imaginary part of the complex resonance frequency is equal to half the bandwidth (see, for example, Section 4.1.3 in Ref. [22]). Note, however, that coupled resonances often are highly damped. γ_P should therefore not be viewed as the bandwidth.

Inserting Eq. (4) into Eq. (2) and using the small load approximation (Eq. (1)), one finds

$$\frac{\Delta\tilde{f}}{f_F} = \frac{N_P}{A}\frac{-\omega M_P}{\pi Z_q}\frac{\tilde{\omega}_P^2}{\tilde{\omega}_P^2 - \omega^2} \tag{6}$$

Δf and $\Delta\Gamma$ plotted versus ω form a resonance curve on their own, hence the name "coupled resonance". The real and the imaginary parts of Eq.
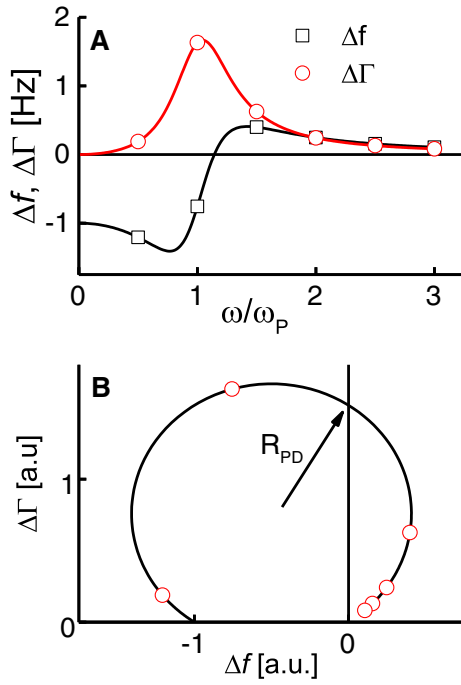
Fig. 2. A: When the sample gives rise to a coupled resonance, Δf and $\Delta\Gamma$ displayed versus overtone order themselves look like a resonance curve. Displayed in polar form, they yield a spiral (B). Squares and circles were inserted to remind the reader that ω can only acquire discrete values, given by the overtones. For this example, γ_P was chosen as $0.3\omega_P$.

(6) are

$$\frac{\Delta f}{f_F} = \frac{N_P}{A} \frac{-\omega M_P}{\pi Z_q} \frac{\omega_P(\omega_P^2 - \omega^2) + (\omega\gamma_P)^2}{(\omega_P^2 - \omega^2)^2 + (\omega\gamma_P)^2}$$

$$\frac{\Delta\Gamma}{f_F} = \frac{N_P}{A} \frac{\omega M_P}{\pi Z_q} \frac{\gamma_P \omega^3}{(\omega_P^2 - \omega^2)^2 + (\omega\gamma_P)^2} \qquad (7)$$

Eqs. (6) and (7) simplify in the limits of large and small ω_P. In the former case (small mass, tight coupling), the Sauerbrey limit is recovered ($\Delta f \approx -2 f_F f N_P M_P/(A Z_q)$). The particles move with the resonator and increase its mass. The opposite limit (large mass, small contact stiffness) leads to elastic coupling [18] ($\Delta f \approx N_P \kappa_P/(2n\pi^2 A Z_q)$). We are interested in the intermediate range ($\omega \sim \omega_P$) in the following. In this range, plots of Δf and $\Delta\Gamma$ versus overtone order (Fig. 2) display certain characteristic features:

— Δf is negative on low harmonics and crosses over to positive values inside the range of frequencies accessible to the QCM (5 to 65 MHz). One can define a "frequency of zero crossing" from interpolation. The frequency of zero crossing can serve as an estimate of the particle resonance frequency, following the relation:

$$f_{ZC} = \frac{1}{2\pi} \omega_P \frac{\omega_P}{\sqrt{\omega_P^2 - \gamma_P^2}}$$

$$= \frac{1}{2\pi} \sqrt{\frac{\kappa_P}{M_P}} \frac{1}{\sqrt{1 - \frac{\xi_P^2}{\kappa_P M_P}}} \qquad (8)$$

Eq. (8) is proven in the appendix. Clearly, the value of γ_P affects the relation between f_{ZC} and ω_P. f_{ZC} only is an estimator of ω_P, it must not be identified with ω_P.

— Close to the zero-crossing frequency, $\Delta\Gamma$ goes through a maximum.
— When plotting $\Delta\Gamma$ versus Δf in a polar diagram, one finds a spiral. In

the limit of small damping, the spiral turns into a circle, but, again, small damping is not usually expected for coupled resonances. As shown in Ref. [23], one can use the radius of the spiral evaluated at $\omega = \omega_P$ (called R_{PD}) as an estimate for the following combination of parameters

$$R_{PD} \approx \frac{1}{2} \Delta\Gamma(\omega = \omega_P) = \frac{N_P}{A} \frac{f_F}{2\pi Z_q} \frac{\kappa_P}{\gamma_P} \qquad (9)$$

Eq. (9) will have to be modified later in order to account for heterogeneity and inefficient coupling. Still, the radius of the circle in the polar diagram is a measure of the contact stiffness, κ_P.

These features are observed in experiment and they can be analyzed, yielding a statement on the stiffness of the bond between the particle and the surface. However, there is a problem with the interpretation of the derived parameters, which has to do with the mode of vibration. Before going into the details, we discuss one data set from Ref. [23] together with a fit with Eq. (5) and show that the derived parameters are inconsistent with what is expected from the experimental conditions.

3. Experimental example

Fig. 3 shows a data set treated in depth in Ref. [23]. The surface of a SiO$_2$-coated resonator had been exposed to a dispersion of glass spheres with radius 0.5 μm. Some of the spheres adsorb to the surface and shift the resonance frequency and the bandwidth. The number of spheres per unit area was determined with a camera. The camera showed that the particles were adsorbed individually. The particles adsorb individually because of their charge. We neglect interparticle interactions in the following discussion. All experiments occurred in aqueous electrolyte solutions. Special about this experiment is the fact that the force of adhesion can be tuned by varying ion concentration. The normal force has three contributions, which are gravity, van-der-Waals (vdW) attraction, and electrostatic repulsion. The electrostatic repulsion is a
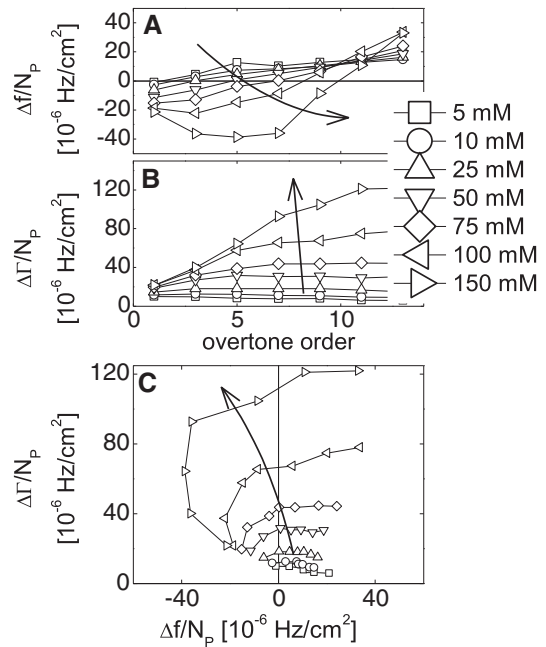

Fig. 3. A and B: $\Delta f/N_P$ and $\Delta\Gamma/N_P$ as a function of the overtone order n. A silica-coated resonator surface had been exposed to glass spheres of radius 0.5 μm. The symbols indicate ionic strength as given in the legend. C: When displayed in polar form, the data form a spiral. They form a circle the limit of small damping.
Adapted from Ref. [23].

consequence of the charge on both silica surfaces. Electrostatic repulsion opposes gravity and vdW attraction. In pure water, the repulsion is so strong that the spheres can be washed away by pumping liquid through the cell. Upon addition of salt, the electrostatic repulsion is screened and the overall attractive force increases. Based on elementary contact-mechanics, the contact stiffness can be expected to follow this increase. The different symbols in Fig. 3 show the different ion strengths. The arrows indicate increasing ionic strength, that is, increasing force of adhesion.

On a phenomenological level the essence of Fig. 3 can be summarized as follows:

— The frequency shift crosses over from negative to positive values within the accessible frequency range. The frequency of zero crossing increases with ion strength. From Eq. (8), this can be interpreted as an increase of contact stiffness with increasing force of adhesion.
— The radius of the circle in the polar diagram also increases with ion strength. Following Eq. (9) this also amounts to an increase of contact stiffness.

Given that the data set from Fig. 3 together with Eqs. (8) and (9) forms a consistent picture, one might hope that quantitatively fitting the data with Eq. (6) was possible and would make the above statements more reliable and exact. There are two separate problems. Firstly, the peaks in bandwidth (Fig. 3B) are too broad to be fitted with Eq. (6). If one makes γ_P large, the coupled resonance becomes asymmetric. With $\gamma_P > \omega_P$, Δf not even turns positive at high overtones. This problem clearly is the consequence of assuming all contacts having equal properties. It can be solved by using the following modified fit function

$$\Delta \tilde{f} = -\frac{N_P}{A}\frac{f_F \omega M_P}{\pi Z_q} \int_0^\infty g(\omega_P) \frac{\omega_P^2 + i\omega\gamma_P}{\omega_P^2 + i\omega\gamma_P - \omega^2}\, d\omega_P + i\Delta\Gamma_{off} \tag{10}$$

$g(\omega_P)$ is a distribution function, assumed to be a Gaussian. An offset in $\Delta\Gamma$ was introduced on a heuristic basis, reasoning that particles should increase the viscous damping exerted by the liquid.

Fig. 4 shows one particular data set together with a prediction from Eq. (10). The open symbols are the data from Fig. 3 with an ion strength of 100 mM. The full line represents the model. The center of the Gaussian distribution for ω_P was at $2\pi \cdot 24$ MHz, the width of the Gaussian was $\sigma = 2\pi \cdot 20$ MHz, the mass was $M_P = 0.19$ pg, the damping factor was $\gamma_P = 2\pi \cdot 4$ MHz, and the offset on the $\Delta\Gamma$ scale was $\Delta\Gamma_{off} = 30$ Hz. Clearly, there are systematic deviations, but these can be removed by the use of distributions of ω_P other than a Gaussian and by also using distributed values of γ_P. There are many different choices for these distributions and many of them are equally reasonable. The outcome of these modeling efforts therefore cannot be unique.

The second problem with quantitative modeling is the value of the parameter M_P. M_P is found to be 0.19 pg in Fig. 4. This value is robust.
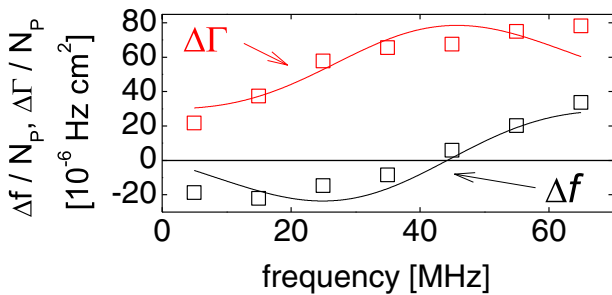

Fig. 4. One of the data sets from Fig. 3 (ion strength of 100 mM, right triangles in Fig. 3) together with an attempt to model the data using Eq. (10). For the parameters see the main text.
Adapted from Ref. [23].

When varying the other parameters of the model, one shifts the features of interest along the frequency scale. The size of the features on the y-axis is largely unaffected. There is little cross-correlation between the optimum value of M_P, on the one hand, and all other fit parameters, on the other.

The number of $M_P \approx 0.19$ pg is too small to be consistent with experiment. The mass of the sphere is given as 1.3 pg (following from a density of 2.5 g/cm^3 and a radius of 0.5 μm). The sphere is embedded in a liquid, which should increase the modal mass because the sphere drags liquid along in its movement. If the sphere undergoes a rotation rather than a translation (see Eq. (13) below), the modal mass should be 2/5 M_P rather than M_P. Still, this factor will not remove the discrepancy between the result from modeling and the true mass. If Eq. (6) shall be made to match the experiment, it must be extended with a prefactor as

$$\frac{\Delta \tilde{f}}{f_F} = -\frac{N_P}{A}f_{OS}\frac{\omega M_P}{\pi Z_q}\frac{\tilde{\omega}_P^2}{\tilde{\omega}_P^2 - \omega^2} \tag{11}$$

The new factor is the "oscillator strength", f_{OS}. The nature of the oscillator strength can be explained invoking an analogy between the coupled resonance and absorption lines in infrared spectroscopy. In IR spectroscopy, the calculation of the oscillator strength involves the transition dipole moment. If the transition dipole moment is zero (that is, if the vibration does not produce an electrical dipole antenna), the vibration does not couple to electromagnetic dipole radiation and therefore is invisible to an IR spectrometer. A coupled resonance is an absorption line in shear-wave spectroscopy. The statement that M_P was smaller than expected can be rephrased to say that the absorption line was weaker than expected. A mode of vibration, which is weakly coupled to the movement of the resonator surface can be reproduced in Finite Element calculations, as shown below.

4. Finite element calculations, multiple modes

The working hypothesis that an adsorbed particle may resonate in more than one way and that these different modes couple to the motion of the resonator to different extents, can be supported with a Finite Element simulation. The simulation amounts to a clean experiment on a computer. The technicalities of the calculation are discussed in Ref. [17]. The user prescribes a geometry, the viscoelastic constants, and the frequency of excitation; the software uses this information to calculate the displacement pattern. The software does not exploit the concept of "modes" or "selection rules". It just solves the underlying partial differential equations. From the displacement pattern, it calculates the area-averaged stress at the resonator surface, which leads to Δf after insertion into the small-load approximation (Eq. (1)). A certain shortcoming of this particular code is that it only works in two dimensions. The circle in Fig. 5 represents an infinite cylinder. It turns out that the motion of the cylinder also displays two resonant modes.

Fig. 5 shows the geometry and the flow field. The resonator surface is located to the left. A particle with a diameter of 4 μm touches the resonator across a link. The link is a rectangle with a thickness of 100 nm and a width of 600 nm. Its shear modulus is 1 GPa. The particle was given a shear modulus of 10 GPa. The way this simulation is set up, the area of the contact remains unchanged if the particle moves. There is neither peeling not sliding.

Fig. 6 shows $\Delta f(f)$ and $\Delta\Gamma(f)$ for frequencies between 1 MHz and 90 MHz. Clearly, there are two coupled resonances, not just one. Moreover, one of the peaks in $\Delta\Gamma(f)$ is smaller than the other. Since we know the displacement patterns, we can look into the question of why the mode at 4.2 MHz is coupled to the resonator's tangential movement less efficiently than the mode at 54 MHz. The Finite Element simulation has solved the mode-assignment problem. The different panels in Fig. 5 correspond to different frequencies, which are 1, 4.2, 54, and 90 MHz. At
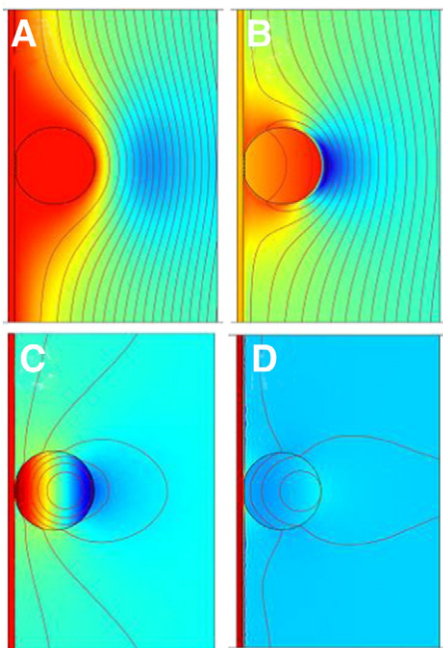
Fig. 5. Displacement pattern around an adsorbed sphere as calculated by the Finite Element Method. The quartz resonator is situated on the left-hand side. The sphere has a diameter of 4 μm and is rigid. It is linked to the substrate across a link with a thickness of 100 nm, a width of 600 nm, and a shear modulus of 1 GPa. The color encodes the local tangential velocity, where red denotes large velocity. For panels A and B, the dark lines are streamlines, where the velocity was is measured relative to the substrate. For panels C and D, the streamlines denote the velocity relative the quiescent liquid at $z = \infty$. The panels on upper left, upper right, lower left, and lower right correspond to oscillation frequencies of 1 MHz, 4.2 MHz, 54 MHz, and 90 MHz, respectively.

low frequencies (1 MHz, panel A), the particle essentially moves with the crystal. The sphere and the trapped liquid increase the resonator's mass, thereby decreasing the resonance frequency. The decrease is about proportional to the frequency itself, as shown on the left-hand side in Fig. 6A. Clearly, this is the Sauerbrey limit. Panel D in Fig. 5 shows the opposite extreme of high frequencies (90 MHz). The particle almost rests in place. It still rotates, but only by a small amount. The link exerts a restoring force onto the resonator, which amounts to elastic coupling as discussed in Ref. [18]. As the right-hand side in Fig. 6A shows, Δf is not positive in this limit, although the frequency shift decreases with increasing ω. Δf is negative because the viscous drag

exerted by the liquid is superimposed onto the force exerted by the sphere. The liquid creates a negative offset. (This effect might be smaller for spheres than for cylinders. This calculation occurred with cylinders.)

Panels B and C show the flow fields at the frequencies of the two resonances (4.2 MHz and 54 MHz). The sphere rotates about the point of contact (or a point close to the contact) at 4.2 MHz, while it rotates about its center (or a point close to that) at 54 MHz. When the sphere rotates about the point of contact, it exerts a torque onto the substrate, rather than a tangential stress, which is why this mode is weakly coupled to the substrate's tangential motion.

5. Representation with a rigid sphere and a deformable link

In the introduction it was emphasized that Dybwad's model is one-dimensional. The Dybwad model leaves open, how the particle moves. The Finite Element Model treats a continuum, which amounts to an infinite number of degrees of freedom. (Of course the number of degrees becomes finite after the simulation space has been covered with a mesh of finite resolution.) In the following, the problem is discussed at an intermediate level of abstraction, where the number of degrees of freedom is large enough to capture multiple modes, but still small enough to allow for a rigorous analytical description. The model of choice is a rigid sphere connected to the surface across a deformable link. The model in a way is close to a mechanical equivalent circuit as shown in Fig. 1B; it differs in that the link is not just a spring, but a rather a rod which can be distorted in different ways. Likewise, the particle is not just a point, but rather a sphere which can undergo translation and rotation. Note: The sphere does not have internal degrees of freedom, it cannot deform. The analytical model here differs from the Finite Element Model, where the sphere was given a shear modulus of 10 GPa. In the Finite Element Model further modes appear at frequencies higher than 90 MHz (not shown in Fig. 6), which correspond to the various modes of internal deformation.

The six ways to deform a link are depicted in Fig. 7A. Three of the modes translate the upper end of the link relative to the bottom, while the three other ones rotate it. The modes are:

- Vertical translation, stretching the link
- In-plane translation along x and y, shearing the link
- Rotation about z, twisting the link
- Rotation of the sphere about horizontal axes (x and y) passing through the link, bending the link.
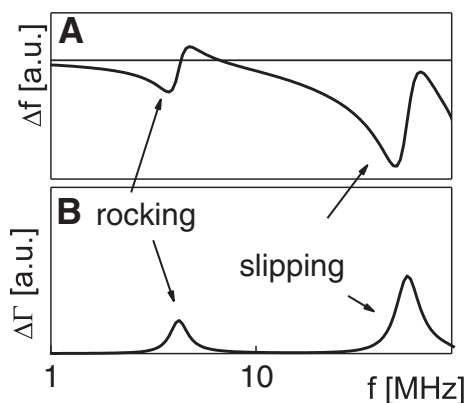

Fig. 6. Shifts of frequency and bandwidth as computed from the Finite Element model shown in Fig. 5. The frequency is on a logarithmic scale. One observes *two* coupled resonances, which are the rocking mode and the slipping mode. The integral over a peak in $\Delta\Gamma(f)$ is proportional to the oscillator strength, f_{OS}.
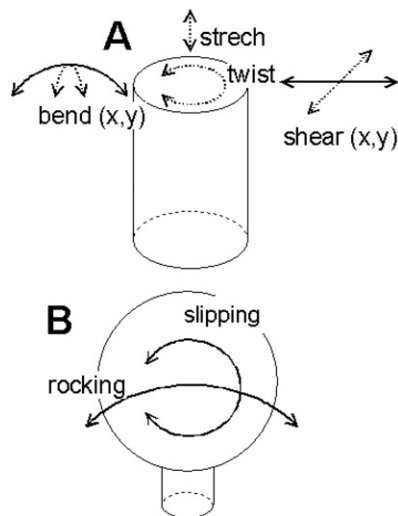

Fig. 7. A link between a particle and a substrate (here displayed as a cylinder) can be deformed from the two ends in 6 different ways (A). Only 2 of those deformations couple to a periodic translation of the substrate along x. These are termed the "slipping mode" and the "rocking mode" (B).

Symmetry imposes certain constraints on the degeneracy (on different modes having the same resonance frequency) and on the selection rules. Because x and y are equivalent, the two modes shearing the bond (along x or y) and the two modes bending the link (along x or y) have the same frequency, respectively. Along similar lines: The substrate performs a translation along x and therefore cannot excite shear along y, bending along y, twist, or the stretching mode. (It was assumed that the substrate is rigid and oscillates along x, like the quartz surface does.) These four modes are forbidden by symmetry. Actually, the stretching mode would become weakly allowed, if there was a normal contribution to the motion of the substrate. There might be such a contribution in real experiments because of energy trapping, but we ignore this possibility in the following. Similarly, shear along y and bending along y will become weakly allowed if the mirror symmetry about the y-axis is broken in some way. This will happen if there is a hydrodynamic interaction between the particle and a second particle in its neighborhood.

The two interesting modes are the one shearing the contact along x and the one bending it along x. These are again depicted in Fig. 7B, where the particle itself was included in the diagram. The modes have been renamed. The link is sheared if the particle performs a rotation about its center. This mode was termed "slipping". ("Slip" here is not meant to denote sliding motion in the sense of tribology. It denotes tangential displacement, opposed by an elastic restoring force.) The link is bent if the particle rotates about an axis passing through the link. This mode was named "rocking" mode. An oscillation of the substrate along x certainly couples to the slipping mode. This mode is allowed. With regard to the rocking mode, the situation is more complicated. One might think that bending of the link would only be induced by a torque, not by a tangential stress. Following this argument, the rocking mode would be forbidden. However, this argument only holds as long as the axis of rotation passes *exactly* through the bond. If the axis of rotation is slightly displaced from the bond, the rocking mode slightly shears the bond and the rocking mode becomes weakly allowed. For the displacement pattern shown in Fig. 5B, the axis of rotation is indeed displaced from the bond and the rocking mode therefore is seen as a weak absorption line in Fig. 6.

The equivalent circuit from Fig. 1B (containing a mass, a spring, and a dashpot) is not invalidated by these insights; it only needs a reinterpretation. Consider the slipping mode, first. The mass must be replaced by a moment of inertia; the force must be replaced by a torque. The moment of inertia of a sphere rotating about its center is $I_P = (2/5) M_P R_P^2$. The torque exerted by the contact is given by $F_0 R_P$ with F_0 the amplitude of the force. The force is equal to $\tilde{\kappa}_{shear} u_0$ and u_0 is related to the angle of rotation, θ_0, as $u_0 = R_P \theta_0$. $\tilde{\kappa}$ was given an index *shear* in order to distinguish it from the bond's bending stiffness. The system obeys the dynamical equation

$$\left(-\omega^2 I_P - \tilde{\kappa}_{shear} R_P^2 \right) \theta_0 = 0 \tag{12}$$

The resonance frequency of the slipping mode follows as

$$\tilde{\omega}_{rot} = \sqrt{\frac{\tilde{\kappa}_{shear} R_P^2}{I_P}} = \sqrt{\frac{5}{2}} \sqrt{\frac{\tilde{\kappa}_{shear}}{M_P}} \tag{13}$$

Rotation can simply be accounted for by a prefactor of $(5/2)^{1/2}$. The factor of $(5/2)^{1/2}$ originates from the relation between mass and moment of inertia. Should the axis of rotation be slightly displaced from the center of the sphere, this shifts the values of I_P and also the calculation of the torque, but the effects are not dramatic.

Now consider the rocking mode. If the axis of rotation is at the point of contact, the moment of inertia is $I_P = 7/5 \, M_P R_P^2$. The torque exerted at the point of contact is equal to the bending stiffness of the

contact, $\tilde{\kappa}_{bend}$, times the angle. The bending stiffness needs to be calculated from contact mechanics. It has units of Nm. The ratio of bending stiffness and moment of inertia has units of s^{-2}. The particle resonance frequency is

$$\tilde{\omega}_{rock} = \sqrt{\frac{5}{7}} \sqrt{\frac{\tilde{\kappa}_{bend}}{M_P R_P^2}} \tag{14}$$

Again, the factor of $(5/7)^{1/2}$ originates from the relation between mass and moment of inertia.

In Fig. 5 the rocking mode occurs at a frequency below the frequency of the slipping mode. This statement holds as long as the radius of contact, a, is much smaller than the particle radius, R_P. For the Hertzian contact with $a \ll R_P$, the shear stiffness and the bending stiffness are

$$\begin{aligned} \kappa_{shear} &= b_{shear} G a \\ \kappa_{bend} &= b_{bend} G a^3 \end{aligned} \tag{15}$$

b_{shear} and b_{bend} are numerical constants of the order of unity. G is the shear modulus. Eq. (15) follows from dimensional arguments. The particle resonance frequencies for the slipping mode and the rocking mode are

$$\begin{aligned} \omega_{rot} &= \sqrt{\frac{\kappa_{shear} R_P^2}{2/5 \; M_P R_P^2}} \approx \sqrt{\frac{5 b_{shear}}{2}} \sqrt{\frac{G a}{M_P}} \\ \omega_{rock} &= \sqrt{\frac{\kappa_{bend}}{7/5 \; M_P R_P^2}} \approx \sqrt{\frac{5 b_{bend}}{7}} \sqrt{\frac{G a}{M_P}} \frac{a}{R_P} \end{aligned} \tag{16}$$

If b_{shear} and b_{bend} are both of order unity and if $a \ll R_P$, the rocking resonance has the lower frequency.

We conclude with an updated equation for the radius of the circle in the polar diagram, R_{PD}. Taking heterogeneous line broadening and the nontrivial oscillator strength into account, the radius becomes

$$R_{PD} \approx f_{OS} \frac{N_P}{A} \frac{f_F}{2\pi Z_q} \frac{\kappa_P}{\gamma_{het}} \tag{17}$$

γ_{het} here is the heterogeneous linewidth, which takes the variability of the contact stiffness between different particles into account.

Unfortunately, it is difficult to experimentally estimate f_{OS}. One would have to know, how far the axis of rotation is displaced from the point of contact. If it is right at the point of contact, f_{OS} is zero because the contact then only exerts a torque. Even if the location of the axis was known, the calculation of the transverse force exerted by the particle's vibration would require a non-trivial calculation, possible involving further unknown parameters.

6. Voigt-type links versus Maxwell-type links

In search of other representations of the link, which are simple, on the hand, and potentially useful in the description of bio-adsorbates, on the other, a second arrangement of a spring and a dashpot comes to mind, which is the Maxwell-type link (Fig. 8B). The Maxwell-type link contains two elements, just like the Voigt-type link (Fig. 8A). Simply adding κ_P to $i\omega\xi_P$ amounts to the Voigt-type link, used in the discussion so far. One might also place the dashpot and the spring in series. This link does not need new free parameters. Computationally, it is almost simple as the Voigt-type link. Considering that the spring and the dashpot are now arranged in parallel, the load impedance from Eq. (2) needs
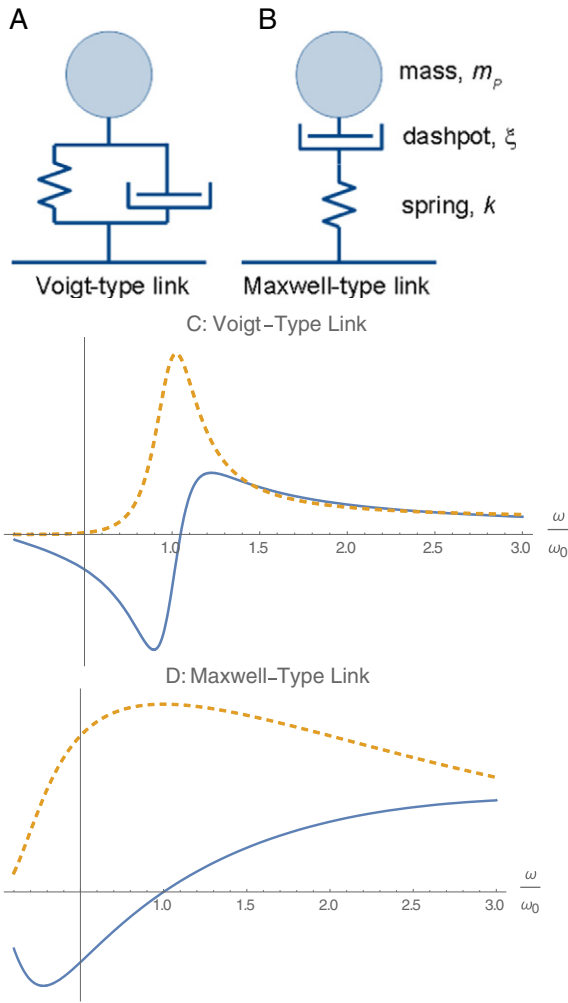
A

B

mass, m_p

dashpot, ξ

spring, k

Voigt-type link　　　　Maxwell-type link

C: Voigt–Type Link

D: Maxwell–Type Link

Fig. 8. Lumped element representations of a particle and a link between the particle and the substrate. The resonator surface is at the bottom. The particle is modeled as rigid. The link is made to be viscoelastic. There is a choice between a parallel and a serial arrangement of the spring and the dashpot (A, B). C, D: Shifts of frequency (Δf, full line) and bandwidth ($\Delta\Gamma$, dashed line) for a Voigt-type link (C) and for a Maxwell-type link (D). The frequency scale was normalized to ω_0. The damping coefficient was set to 0.3 ω_0. So far, the link was modeled a spring and a dashpot arranged in parallel. The complex stiffness of the link was expressed as $\kappa_P + i\omega\xi_P$, where κ_P and ξ_P were assumed to be independent of frequency. For biological colloids like bacteria or viruses, the link between the object under study and the resonator surface will be a complex object, itself. Representing its mechanical properties as in Fig. 1B may or may not be appropriate. In general, the complex stiffness of the link will be some complicated function of frequency. Writing it as $\kappa_P + i\omega\xi_P$ is not more than one particular choice.

to be replaced by

$$\tilde{Z}_{L,Maxwell} = \frac{N_P}{A}\left(\frac{1}{\frac{\kappa_P}{i\omega}} + \frac{1}{\xi_P} + \frac{1}{i\omega M_P}\right)^{-1} \qquad (18)$$

Using $\omega_P^2 = \kappa_P/m_P$ and $\gamma_P = \xi_P/m_P$ as before, one can write

$$\tilde{Z}_{L,Maxwell} = \frac{N_P}{A} i\omega M_P \frac{1}{1 - \frac{\omega^2}{\omega_P^2} + \frac{i\omega}{\gamma_P}} \qquad (19)$$

Eq. (11) is recovered if one writes $\tilde{\omega}_P$ as

$$\tilde{\omega}_P^2 = \frac{1}{M_P}\left(\frac{1}{\kappa_P} + \frac{1}{i\omega\xi_P}\right)^{-1} \qquad (20)$$

The latter relation needs to be compared to Eq. (4). Note that the parameter $\tilde{\omega}_P$ in both cases depends on ω. Panels C and D in Fig. 8 show the derived shifts of frequency and bandwidth. Clearly, the Maxwell-type link yields much broader absorption lines, which is in agreement with recent experiments [24].

7. Discussion

Both Finite Element Simulation and the analytical treatment in Section 5 show that a QCM experiment amounts to shear-wave spectroscopy. The analysis is appealing because it connects different branches of physics, in this case vibrational spectroscopy and acoustic sensing. Beauty of the argument and educational value aside: Does this analysis change the way, how we do acoustic sensing; does it open up new opportunities? Clearly, one has to be careful not to raise false expectations. The seminal paper, which opened up new avenues for sensing was Dybwad's paper from 1985 [20]. Dybwad showed that a contact stiffness can be measured with a QCM. A routine methodology to determine the stiffness between bio-colloids and solid surfaces would be extremely valuable. The operation of the QCM is routine and the QCM averages over the acoustically active area. Averaging is an important advantage. There is no need to pull on single objects or to mechanically actuate them in any way (as this is done in scanning force microscopy [25] and with the colloidal force probe [26]). There is no need to repeat experiments many times in order to obtain a meaningful average of contact strength or contact stiffness. Contact mechanics with a QCM - if it works – will be very useful.

At this point, it is not clear, how well QCM-based contact mechanics can work on bio-colloids. What are the limits? Why is it difficult? Below are some thoughts.

- Contact mechanics does work fairly well (both in liquids and in air) if the object under study is so large that it is held in place by inertia. Typical objects of this type would be millimeter-sized glass spheres. Possibly, the most promising route towards QCM-based biomechanics is to place the sample of interest between the resonator surface and such a large sphere. This might give an easier access to mechanical stiffness of biocolloids than the coupled resonance.
- The analysis of experiments is easier in air than in liquids because hydrodynamic effects cannot be accounted for easily. However, the scientific problems are less interesting because the forces tend to be non-specific (van-der-Waals forces, capillary forces).
- Quantitative determination of the contact stiffness is difficult because the prefactor f_{OS} in Eq. (11) (the "oscillator strength") is not usually known. However, the prefactor cancels in the analysis of the loss tangent, given as $\tan(\delta) = \omega\xi_P/\kappa_P$. The loss tangent *can* be quantitatively inferred from the experimental data.
- Even using the simplest representations of the link, there is an interesting choice between placing the spring and the dashpot in parallel (as in the Voigt-type link) or in series (as in the Maxwell-type link). These two arrangements can be distinguished, experimentally, from the overtone-dependence of Δf and $\Delta\Gamma$.
- Realistic numeric modeling of surface-adsorbed particles in 3D accounting for hydrodynamics is under way [27]. This will allow for a detailed quantitative comparison between theory and experiment, at least for well-defined model systems.
- If one relies on the coupled resonance, the zero-crossing frequency must be in the accessible frequency window for the method to work. If the mass of the particle can be chosen at will, the zero-crossing frequency can be moved towards the frequency window of the QCM. This would usually require spheres of some kind to be a central component of the sample. Glass spheres (even with special surface functionalization) often are available in different sizes.
- Spheres as a central component of the sample should always be helpful in that they provide for a clean geometry. Experiments with coupled resonances using bacteria have been done [28], but

the quantitative analysis is more difficult than with glass spheres.

- Well-defined substrates should also be helpful. Possibly, supported lipid membranes (SLBs, Ref. [29]) can make a difference.
- Tuning the interaction in whatever way should make data interpretation easier. Electrostatic forces were used in Ref. [23]. Vollmer and co-workers have used a QCM combined with a centrifuge for a similar purpose [30].
- As always, combining the QCM with some other surface-analytical technique (such as microscopy or electrochemical impedance analysis) might help.

While one can be optimistic with regard to future progress, there of course is a central message from this analysis, which is relevant today: it is more complicated than one might think. Translation and rotation both come into play. Also: Experiments can only be understood if the imperfect coupling (quantified by the oscillator strength) is accounted for.

8. Conclusions

There is a close analogy between QCM-based sensing and vibrational spectroscopy. The QCM can perform vibrational spectroscopy on surface-adsorbed colloidal particles. The analysis shows that two separate modes exist, where the first is a rotation about the point of contact and the second is a rotation about the center of the particle. These two modes are connected to the bond's bending stiffness and the bond's shear stiffness, respectively. The most important consequence for the contact resonance model is that a prefactor must be introduced (an "oscillator strength") which accounts for imperfect coupling between the resonator and the sample.

Acknowledgements

Appendix A. Proof of Eq. (8)

At the frequency of zero-crossing, $f_{ZC} = \omega_{ZC}/(2\pi)$, the real part of Eq. (6) to become zero. Ignoring the real prefactors, we have

$$
\begin{aligned}
\frac{\tilde{\omega}_P^2}{\tilde{\omega}_P^2 - \omega_{ZC}} &= \frac{\omega_P^2 + i\omega_{ZC}\gamma_P}{\omega_P^2 + i\omega_{ZC}\gamma_P - \omega_{ZC}^2} \\
&= \frac{\left(\omega_P^2 + i\omega_{ZC}\gamma_P\right)\left(\left(\omega_P^2 - \omega_{ZC}^2\right) - i\omega_{ZC}\gamma_P\right)}{\left(\omega_P^2 - \omega_{ZC}^2\right)^2 + \left(\omega_{ZC}\gamma_P\right)^2}
\end{aligned}
\tag{21}
$$

ω_P^2 here is the real part of $\tilde{\omega}_{P2}$. The real part of this expression turns to zero if the real part of the numerator is zero:

$$
0 = \omega_P^2\left(\omega_P^2 - \omega_{ZC}^2\right) + \left(\omega_{ZC}\gamma_P\right)^2 = \omega_P^4 + \omega_{ZC}^2\left(\gamma_P^2 - \omega_P^2\right)
\tag{22}
$$

Solving for ω_{ZC} and only accepting the positive solutions, we obtain

$$
\omega_{ZC} = 2\pi f_{ZC} = \frac{\omega_P^2}{\sqrt{\omega_P^2 - \gamma_P^2}}
\tag{23}
$$

References

[1] C. Lu, A.W. Czanderna, Applications of Piezoelectric Quartz Crystal Microbalances, Elsevier, Amsterdam, 1984.
[2] C. Steinem, A. Janshoff, Piezoelectric Sensors, Springer, Heidelberg, 2007.
[3] D. Johannsmann, Viscoelastic, mechanical, and dielectric measurements on complex samples with the quartz crystal microbalance, Phys. Chem. Chem. Phys. 10 (31) (2008) 4516–4534.
[4] R. Beck, U. Pittermann, K.G. Weil, Impedance analysis of quartz oscillators, contacted on one side with a liquid, Ber. Bunsenges. Phys. Chem. Chem. Phys. 92 (11) (1988) 1363–1368.
[5] H.L. Bandey, S.J. Martin, R.W. Cernosek, A.R. Hillman, Modeling the responses of thickness-shear mode resonators under various loading conditions, Anal. Chem. 71 (11) (1999) 2205–2214.
[6] D. Johannsmann, Viscoelastic analysis of organic thin films on quartz resonators, Macromol. Chem. Phys. 200 (3) (1999) 501–516.
[7] A. Pomorska, D. Shchukin, R. Hammond, M.A. Cooper, G. Grundmeier, D. Johannsmann, Positive frequency shifts observed upon adsorbing micron-sized solid objects to a quartz crystal microbalance from the liquid phase, Anal. Chem. 82 (6) (2010) 2237–2242.
[8] M. Berglin, A. Olsson, H. Elwing, The interaction between model biomaterial coatings and nylon microparticles as measured with a quartz crystal microbalance with dissipation monitoring, Macromol. Biosci. 8 (5) (2008) 410–416.
[9] J. Fatisson, R.F. Domingos, K.J. Wilkinson, N. Tufenkji, Deposition of TiO(2) nanoparticles onto silica measured using a quartz crystal microbalance with dissipation monitoring, Langmuir 25 (11) (2009) 6062–6069.
[10] V. Heitmann, B. Reiss, J. Wegener, The quartz crystal microbalance in Cell biology: basics and applications, in: C. Steinem, A. Janshoff (Eds.), Piezoelectric Sensors, Springer, 2007.
[11] C.A. Keller, B. Kasemo, Surface specific kinetics of lipid vesicle adsorption measured with a quartz crystal microbalance, Biophys. J. 75 (3) (1998) 1397–1402.
[12] F.N. Dultsev, R.E. Speight, M.T. Florini, J.M. Blackburn, C. Abell, V.P. Ostanin, D. Klenerman, Direct and quantitative detection of bacteriophage by "hearing" surface detachment using a quartz crystal microbalance, Anal. Chem. 73 (16) (2001) 3935–3939.
[13] M.A. Cooper, F.N. Dultsev, T. Minson, V.P. Ostanin, C. Abell, D. Klenerman, Direct and sensitive detection of a human virus by rupture event scanning, Nat. Biotechnol. 19 (9) (2001) 833–837.
[14] A.L.J. Olsson, H.C. van der Mei, H.J. Busscher, P.K. Sharma, Influence of cell surface appendages on the bacterium-substratum interface measured real-time using QCM-D, Langmuir 25 (3) (2009) 1627–1632.
[15] A.C. Olofsson, M. Hermansson, H. Elwing, Use of a quartz crystal microbalance to investigate the antiadhesive potential of N-acetyl-L-cysteine, Appl. Environ. Microbiol. 71 (5) (2005) 2705–2712.
[16] E.V. Olsen, S.T. Pathirana, A.M. Samoylov, J.M. Barbaree, B.A. Chin, W.C. Neely, V. Vodyanoy, Specific and selective biosensor for Salmonella and its detection in the environment, J. Microbiol. Methods 53 (2) (2003) 273–285.
[17] E. Tellechea, D. Johannsmann, N.F. Steinmetz, R.P. Richter, I. Reviakine, Model-independent analysis of QCM data on colloidal particle adsorption, Langmuir 25 (9) (2009) 5177–5184.
[18] A. Laschitsch, D. Johannsmann, High frequency tribological investigations on quartz resonator surfaces, J. Appl. Phys. 85 (7) (1999) 3759–3765.
[19] J.N. D'Amour, J.J.R. Stalgren, K.K. Kanazawa, C.W. Frank, M. Rodahl, D. Johannsmann, Capillary aging of the contacts between glass spheres and a quartz resonator surface, Phys. Rev. Lett. 96 (5) (2006) 058301.
[20] G.L. Dybwad, A sensitive new method for the determination of adhesive bonding between a particle and a substrate, J. Appl. Phys. 58 (7) (1985) 2789–2790.
[21] M. Rodahl, F. Hook, C. Fredriksson, C.A. Keller, A. Krozer, P. Brzezinski, M. Voinova, B. Kasemo, Simultaneous frequency and dissipation factor QCM measurements of biomolecular adsorption and cell adhesion, Faraday Discuss. 107 (1997) 229–246.
[22] D. Johannsmann, The Quartz Crystal Microbalance in Soft Matter Research: Fundamentals and Modeling, Springer, 2015.
[23] A.L.J. Olsson, H.C. van der Mei, D. Johannsmann, H.J. Busscher, P.K. Sharma, Probing colloid-substratum contact stiffness by acoustic sensing in a liquid phase, Anal. Chem. 84 (10) (2012) 4504–4512.
[24] R. van der Westen, H.C. van der Mei, H.J. Busscher, P.K. Sharma, H.A. de Raedt, private communication, 2016.
[25] M. Rief, F. Oesterhelt, B. Heymann, H.E. Gaub, Single molecule force spectroscopy on polysaccharides by atomic force microscopy, Science 275 (5304) (1997) 1295–1297.
[26] H.J. Butt, B. Cappella, M. Kappl, Force measurements with the atomic force microscope: technique, interpretation and applications, Surf. Sci. Rep. 59 (1-6) (2005) 1–152.
[27] D. Johannsmann, G. Brenner, Frequency shifts of a quartz crystal microbalance calculated with the frequency-domain lattice-Boltzmann method: application to coupled liquid mass, Anal. Chem. 87 (14) (2015) 7476–7484.
[28] A.L.J. Olsson, N. Arun, J.S. Kanger, H.J. Busscher, I.E. Ivanov, T.A. Camesano, Y. Chen, D. Johannsmann, H.C. van der Mei, P.K. Sharma, The influence of ionic strength on the adhesive bond stiffness of oral streptococci possessing different surface appendages as probed using AFM and QCM-D, Soft Matter 8 (38) (2012) 9870–9876.
[29] R.P. Richter, R. Berat, A.R. Brisson, Formation of solid-supported lipid bilayers: an integrated view, Langmuir 22 (8) (2006) 3497–3505.
[30] A. Webster, F. Vollmer, Y. Sato, Probing biomechanical properties with a centrifugal force quartz crystal microbalance, Nat. Commun. 5 (2014) 5284.